Finite-element analysis of electron-hydrogen scattering

J. Shertzer
Department of Physics, College of the Holy Cross, Worcester, Massachusetts 01610

J. Botero
Division of Physical Sciences, International Atomic Energy Agency, Vienna, Austria

(Received 6 December 1993)

The Schrödinger equation for electron-hydrogen scattering is solved directly using finite-element analysis. Below the $n=2$ threshold, accurate phase shifts for $0 \le L \le 3$ are obtained and compared with variational and R-matrix results. Resonance positions and widths are also calculated and are in good agreement with other theoretical values. Above the $n=2$ threshold, partial-wave contributions to the cross sections $\sigma_{1s\text{-}1s}$, $\sigma_{1s\text{-}2s}$, and $\sigma_{1s\text{-}2p}$ are calculated and compared with those obtained using close-coupling and R-matrix methods. Wave functions are shown for both elastic and multichannel scattering.

PACS number(s): 34.80.Bm, 34.80.Dp

I. INTRODUCTION

The finite-element method (FEM) offers an alternate approach for studying few-body systems by allowing one to obtain a direct solution of the Schrödinger equation for both bound and continuum states [1]. Recently, we reported preliminary results on the elastic scattering of electrons from hydrogen using the FEM [2]. In this paper, we give details of the calculation and show that the method can be extended to the multichannel problem by simply modifying the boundary conditions. We present inelastic cross sections above the $n=2$ threshold and compare FEM results with R-matrix and close-coupling calculations.

In the more conventional approaches to scattering, such as variational, R-matrix, or close-coupling methods, one constructs an approximate wave function using a global basis set, such as the hydrogenic states. In finite-element analysis, one approximates the wave function piecewise using simple polynomial functions. This has the advantage of providing greater flexibility in simulating the behavior of the wave function in both the interaction and asymptotic region. Another advantage of the finite-element method is the ease with which one can impose complicated boundary conditions. This feature makes it ideal for treating multichannel scattering. The major limitation to the finite-element method is that it becomes computationally prohibitive for more than two electrons. Nevertheless, one could use this approach to study electron scattering from the alkali metals by introducing an effective potential; the method can also be readily adapted to study electron scattering from He^+.

The problem of electron-hydrogen scattering has a long history. Although the system is relatively simple in that it contains only three charged particles, it nevertheless has all the complexities of multichannel scattering: there are series of resonances below each threshold and the number of physically open channels is infinite at the ionization threshold. For these reasons, it has been the subject of many theoretical and experimental investigations. Although electron-hydrogen scattering has been treated successfully by variational, R-matrix, and close-coupling methods, no single calculation can yield accurate scattering parameters over a wide energy range and there is still some disagreement between various calculations in the regimes where the results overlap, particularly at higher energies. It is hoped that through a direct solution of the Schrödinger equation, finite-element analysis will provide a tool for studying scattering that is accurate over a wide range of energy. However, we are still far from that goal; the purpose of this paper is merely to demonstrate that the method can be used for elastic and inelastic scattering, and in the energy region studied to date, there is excellent agreement with other theoretical calculations.

In the next section we outline the procedure for using the FEM for elastic scattering. We present elastic phase shifts and resonance positions and widths below the $n=2$ threshold, as well as wave functions for both the resonant and nonresonant case. In Sec. III we extend the analysis to multichannel scattering and examine the scattering region where the $2s$ and $2p$ channels are open. We compare FEM results for inelastic cross sections and eigenphase sums with close-coupling and R-matrix results. Concluding remarks are given in Sec. IV.

II. FINITE-ELEMENT ANALYSIS OF ELASTIC SCATTERING

A. Description of the algorithm

The two-electron Schrödinger equation (in atomic units) is

$$\left[-\frac{\nabla_1^2}{2}-\frac{\nabla_2^2}{2}-\frac{1}{r_1}-\frac{1}{r_2}+\frac{1}{r_{12}}-E\right]\Psi(\mathbf{r}_1,\mathbf{r}_2)=0\ ; \quad (2.1)$$

solutions of Eq. (2.1) are identified by their total angular momentum L, spin S, and parity π; for scattering states, the parity is determined once L and S have been specified. The wave function $\Psi^{LS}(\mathbf{r}_1,\mathbf{r}_2)$ is first expanded in coupled spherical harmonics,

$$\Psi^{LS}(\mathbf{r}_1,\mathbf{r}_2)=\sum_{l_1,l_2} U^{LS}_{l_1 l_2}(r_1,r_2)\,Y^{LM}_{l_1 l_2}(\hat{\mathbf{r}}_1,\hat{\mathbf{r}}_2)\ . \quad (2.2)$$

All of the angular dependence of the wave function is accounted for through the spherical harmonics; the values of l_1 and l_2 retained in the sum for $0 \le L \le 3$ are

$L=0$		$L=1$		$L=2$		$L=3$	
l_1	l_2	l_1	l_2	l_1	l_2	l_1	l_2
0	0	1	0	2	0	3	0
1	1	0	1	0	2	0	3
2	2	2	1	3	1	4	1
3	3	1	2	1	3	1	4
		2	3	1	1	2	1
		3	2	2	2	1	2

Substituting Eq. (2.2) into Eq. (2.1), we obtain a set of coupled differential equations for the radial functions $U^{LS}_{l_1 l_2}$,

$$\sum_{l_1,l_2} H^{L}_{l_1' l_2', l_1 l_2} U^{LS}_{l_1 l_2}(r_1,r_2)=0 , \tag{2.3}$$

where

$$H^{L}_{l_1' l_2', l_1 l_2} = \sum_{i=1}^{2} \left[-\frac{1}{2}\frac{\partial^2}{\partial r_i^2} - \frac{1}{r_i}\frac{\partial}{\partial r_i} + \frac{l_i(l_i+1)}{2r_i^2} - \frac{1}{r_i} - \frac{E}{2} \right] \delta_{l_1',l_1}\delta_{l_2',l_2} + \sum_{k=0}^{\infty} \frac{r_<^k}{r_>^{k+1}} \langle Y^{LM}_{l_1' l_2'}(\hat{\mathbf{r}}_1,\hat{\mathbf{r}}_2) | P_k(\cos\theta_{12}) | Y^{LM}_{l_1 l_2}(\hat{\mathbf{r}}_1,\hat{\mathbf{r}}_2) \rangle . \tag{2.4}$$

The angular brackets indicate integration over the angular coordinates and $E=-\frac{1}{2}+k^2/2$ is the total energy, where k is the incident momentum of the electron and the hydrogen target is in the ground state. Note that all of the coupling between states with different l_1, l_2 comes from the electron-electron interaction. The radial functions $U^{LS}_{l_1 l_2}$ are obtained by solving Eq. (2.3) with the FEM.

In finite-element analysis, the coordinate space spanned by r_1 and r_2 is truncated and discretized into small regions called elements [1]. The cutoff r_c must be chosen large enough so that one can impose the asymptotic boundary condition at $r_1=r_c$ and $r_2=r_c$. The size of the elements may vary, and in general one uses smaller elements in regions where the potential is strong and the function is expected to have a lot of structure, and larger elements where the wave function is smooth and the probability density is small.

In each element ε, we seek a solution of the coupled radial equations; the radial functions $U^{LS}_{l_1 l_2}$ are expanded in a local basis set

$$U^{LS(\varepsilon)}_{l_1 l_2}(r_1,r_2)=\sum_{i=1}^{36} u^{LS(\varepsilon)}_{l_1 l_2 i}\phi^{(\varepsilon)}_i(r_1,r_2) . \tag{2.5}$$

The functions $\phi^{(\varepsilon)}_i(r_1,r_2)$ are products of fifth degree polynomials in r_1 and r_2 and are nonzero only in element ε. These basis functions have the unique property that the 36 expansion coefficients $u^{LS(\varepsilon)}_{l_1 l_2 i}$ are the value of the function $U^{LS}_{l_1 l_2}$ and its derivatives $\partial U^{LS}_{l_1 l_2}/\partial r_1$, $\partial U^{LS}_{l_1 l_2}/\partial r_2$, and $\partial^2 U^{LS}_{l_1 l_2}/\partial r_1 \partial r_2$ at nine nodes in the element; the nodes are located at the four corners, the midpoints of the sides, and the center of the element. It is this particular feature of the finite-element method that allows one to impose either bound or continuum state boundary conditions with relative ease. Substituting Eq. (2.5) into Eq. (2.3) and projecting onto the local basis functions, we obtain a set of coupled linear equations for the expansion coefficients for element ε:

$$H^{L(\varepsilon)} u^{LS(\varepsilon)}=0 , \tag{2.6}$$

where

$$H^{L(\varepsilon)}_{i l_1' l_2', l_1 l_2 j} = \langle \phi^{(\varepsilon)}_i(r_1,r_2) | H^{L}_{l_1' l_2', l_1 l_2} | \phi^{(\varepsilon)}_j(r_1,r_2) \rangle . \tag{2.7}$$

The angular brackets here indicate integration over the area of element ε. Since the diagonal matrix elements involve only simple polynomials, all of the integrations can be done exactly with eight-point Gauss quadrature. For the off-diagonal terms, we also used eight-point Gauss quadrature except for elements along the diagonal $r_1=r_2$, where the quadrature was increased to 16 points. The local matrices are symmetric and of order 144 for $L=0$ and 216 for $L\geq 1$.

Local equations of the form Eq. (2.6) are generated for each element ε, but are not solved independently. The expansion coefficients for nodes that lie on the boundary between two or four elements couple together the local equations for those elements. That is, if $u^{LS(\varepsilon)}_{l_1 l_2 i}$ and $u^{LS(\varepsilon')}_{l_1 l_2 i'}$ correspond to the value of the radial function at a common node on the boundary between elements ε and ε', those two coefficients must be equal if the function is to be continuous across the element boundary. Thus the coupling of the equations ensures continuity of the functions (and derivatives) across the element boundaries.

The local matrices are "added" together to form a single global matrix

$$\sum_{\varepsilon} H^{L(\varepsilon)} u^{LS(\varepsilon)} = H^{L} u^{LS}=0 . \tag{2.8}$$

The global matrix is banded and symmetric, and a single global matrix element may contain contributions from one, two, or four local matrices. The components of the vector u^{LS} are the yet undetermined values of the radial functions and derivatives at all the nodes in the (r_1,r_2) grid.

The global matrix is independent of the spin S. We can now use the symmetry properties of the singlet and triplet state to reduce the size of the global matrix by a factor of 2. Under exchange of the two electrons, the radial functions must obey

$$P_{12} U^{LS}_{l_1 l_2}(r_1,r_2)=(-1)^S U^{LS}_{l_2 l_1}(r_2,r_1) . \tag{2.9}$$

Consequently, we can solve the finite-element equations on the half-grid $r_1 \geq r_2$ and require that the singlet and triplet radial functions satisfy Eq. (2.9); this imposes a constraint on certain components of the vector u^{LS} that correspond to nodes with $r_1 = r_2$.

The asymptotic scattering boundary condition must now be imposed at $r_1 = r_c$. For elastic scattering, the radial functions $U^{LS}_{l_1 l_2}$ are given asymptotically by

$$U^{LS}_{l_1 l_2}(r_1, r_2) = \delta_{l_1, L}\delta_{l_2, 0} R_{10}(r_2)\sqrt{k} \times [j_L(kr_1) + \tan\delta_L j_{-L-1}(kr_1)] , \quad (2.10)$$

where j_L is the spherical Bessel function, R_{10} is the $1s$ hydrogen radial function, and δ_L is the elastic phase shift. [The values of the derivatives on the boundary can be obtained by differentiating Eq. (2.10).]

The indices for the global matrix (of order N) given in Eq. (2.8) can be arranged such that the first n components of u^{LS} correspond to the value of the radial functions and derivatives at interior nodes and the last $(N-n)$ components are associated with nodes on the boundary. These boundary components are determined by Eq. (2.10) up to a common phase shift. We cast the global matrix equation into a new form

$$\tilde{H}^L \tilde{u}^{LS} = \tilde{c}^{LS} , \quad (2.11)$$

where

$$\begin{aligned} &\tilde{H}^L_{ij} = H^L_{ij}, \quad 1 \leq i \leq n+1, \ 1 \leq j \leq n \\ &\tilde{u}^{LS}_j = u^{LS}_j, \quad 1 \leq j \leq n \\ &\tilde{u}^{LS}_{n+1} = \tan\delta_L , \\ &\tilde{H}^L_{i,n+1}\tilde{u}^{LS}_{n+1} - \tilde{c}^{LS}_i = \sum_{j=n+1}^{N} H^L_{ij} u^{LS}_j, \quad 1 \leq i \leq n+1 . \end{aligned} \quad (2.12)$$

The matrix $\tilde{H}$ is of order $(n+1)$ and the last component of the vector $\tilde{u}^{LS}$ is the unknown phase shift. The matrix $\tilde{H}^L$ is inverted to obtain the radial functions and the unknown phase shift using standard routines for Gaussian elimination of banded matrices.

B. Results for elastic phase shifts

The finite-element results for the elastic phase shifts were obtained on a 10×10 grid, with $r_c = 40a_0$ for $k = 0.1$ and 0.2, and $r_c = 24a_0$ for $0.3 \leq k \leq 0.8$. No attempt was made to optimize the grid at each run. In the interaction region, we used six elements with boundaries at $0a_0$, $0.25a_0$, $0.5a_0$, $1a_0$, $2a_0$, $4a_0$, and $8a_0$; between $8a_0$ and r_c, we used four additional elements of size $4a_0$ or $8a_0$, depending on the wavelength in the asymptotic region. The CPU time on an IBM ES/9000 computer was 1.0 min per phase shift for $L = 0$ and 1.5 min for $L \geq 1$. Unlike the variational method, the computational effort does not steadily increase as a function of L. The

TABLE I. Singlet and triplet elastic phase shifts. Finite-element results are compared with R-matrix [7], variational [3–6], and finite-difference [8] calculations.

State	Method \ k (a.u.)	0.1	0.2	0.3	0.4	0.5	0.6	0.7	0.8
$^1S^e$	R-matrix	2.550	2.062	1.691	1.410	1.196	1.035	0.925	
	variational	2.553	2.067	1.696	1.415	1.202	1.041	0.930	0.886
	finite-difference	2.555	2.067	1.696	1.415	1.201	1.041	0.930	0.887
	finite-element	2.553	2.066	1.695	1.414	1.200	1.040	0.930	0.887
$^3S^e$	R-matrix	2.939	2.717	2.500	2.294	2.105	1.933	1.780	
	variational	2.939	2.717	2.500	2.294	2.105	1.933	1.780	1.643
	finite-difference	2.939	2.717	2.500	2.294	2.104	1.933	1.780	1.646
	finite-element	2.938	2.717	2.500	2.294	2.104	1.933	1.780	1.645
$^1P^o$	R-matrix	0.006	0.015	0.016	0.009	−0.002	−0.012	−0.016	
	variational	0.007	0.015	0.017	0.010	−0.001	−0.009	−0.013	−0.004
	finite-element	0.006	0.015	0.016	0.009	−0.002	−0.012	−0.015	−0.007
$^3P^o$	R-matrix	0.010	0.045	0.107	0.187	0.270	0.341	0.392	
	variational	0.011	0.045	0.106	0.187	0.271	0.341	0.393	0.427
	finite-element	0.010	0.045	0.107	0.187	0.271	0.342	0.393	0.428
$^1D^e$	R-matrix	0.0013	0.0051	0.011	0.018	0.027	0.038	0.052	
	variational	0.0012	0.0052	0.011	0.018	0.027	0.038	0.052	0.075
	finite-element	0.0007	0.0048	0.011	0.018	0.027	0.038	0.052	0.074
$^3D^e$	R-matrix	0.0013	0.0052	0.011	0.020	0.030	0.042	0.055	
	variational	0.0013	0.0052	0.011	0.020	0.030	0.042	0.055	0.070
	finite-element	0.0007	0.0049	0.011	0.020	0.030	0.042	0.055	0.070
$^1F^o$	variational			0.0038	0.0066	0.010	0.015	0.020	0.026
	finite-element	0.0000	0.0016	0.0037	0.0065	0.010	0.015	0.020	0.026
$^3F^o$	variational			0.0038	0.0067	0.010	0.015	0.020	0.026
	finite-element	0.0000	0.0016	0.0037	0.0065	0.010	0.015	0.020	0.027

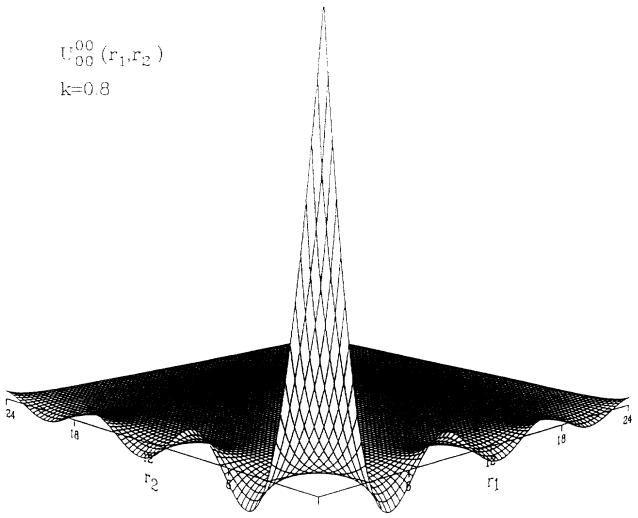

FIG. 1. Radial function U_{00}^{00} at $k=0.8$ (a.u.); r_1 and r_2 are in units of a_0.

results were stable with respect to increasing r_c, increasing the number of elements and increasing the number of angular basis functions. The FEM results are compared with variational [3–6] and R-matrix [7] results in Table I; also included for $L=0$ are the recent numerical results of Wang and Callaway [8], who used a finite-difference propagation scheme.

The radial function U_{00}^{00} at $k=0.8$ is shown in Fig. 1. This function is symmetric about the diagonal and is the only radial function that does not vanish asymptotically. U_{00}^{00} is about a factor of 10 larger in magnitude than the other functions $U_{l_1 l_2}^{00}$, which contribute to the total $^1S^e$ scattering wave function. Figure 1 is typical of the entire nonresonant scattering region, $0 \le k \le 0.8$. In all cases, $0 \le L \le 3$, the total wave function was dominated by the contribution of the states U_{L0}^{LS} and U_{0L}^{LS}; this is consistent with the rapid convergence of the results with respect to the number of angular states retained in the expansion in Eq. (2.1).

C. Resonances below the $n=2$ threshold

In the energy region $0.8 < k < 0.886$ ($k=0.886$ is the $n=2$ threshold), there are a series of resonances corresponding to quasistable doubly excited states of H^-. As one passes through a resonance, the phase shift undergoes an abrupt change of π; this resonant behavior is superimposed on the general background behavior of the phase shift as a function of k. To a good approximation, the resonance can be fit to

$$\tan(\delta-\delta_0)=\frac{\Gamma}{2(E_R-E)}\ , \tag{2.13}$$

where E_R is the resonant energy, Γ is the width, and δ_0 is the background value of the phase shift, which is assumed to be constant over Γ.

We calculated the position and width of the lowest-lying resonance for each partial wave using a three point fit to Eq. (2.13). CPU times were under 2 min for $L=0$ and under 5 min for $L \ge 1$, using a 14×14 grid with $r_c=40a_0$. We compare these results with R-matrix calculations [7] and the complex coordinate rotation results [9] in Table II. [The values for the positions and widths given in Table II are slightly improved over those in Ref. [2], where a two-point fit to Eq. (2.13) was used with an approximate value of δ_0.]

TABLE II. Resonances below the $n=2$ threshold. Finite-element results are compared with the R-matrix method [7] and complex-coordinate rotation method (CCRM) [9].

State	Method	Position (eV)	Width (eV)
$^1S^e$	R-matrix	9.5572	0.0471
	CCRM	9.5574	0.0471
	finite-element	9.5573	0.0472
$^3P^o$	R-matrix	9.7382	0.0058
	CCRM	9.7381	0.0058
	finite-element	9.7382	0.0058
$^1D^e$	R-matrix	10.125	0.0088
	CCRM	10.124	0.0086
	finite-element	10.128	0.0093

In Fig. 2 we show the radial function U_{00}^{00} at $k=0.838$, which lies within the width of the lowest $^1S^e$ resonance. Although the radial functions at $k=0.8$ (Fig. 1) and $k=0.838$ were obtained using the identical boundary conditions, the structure of the functions is dramatically different. The behavior associated with a doubly excited state is clearly observable at the resonant energy. The "bound-state" part of the radial function is much more extended in space than its nonresonant counterpart and the amplitude of the wave function along the diagonal $r_1=r_2$ is significantly greater.

Clearly, the finite-element method is successful for single channel elastic scattering. In the next section, we describe how this procedure can be extended to treat multichannel scattering.

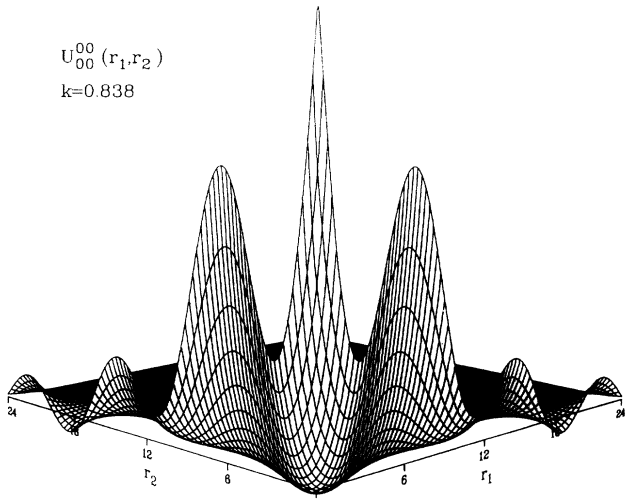

FIG. 2. Radial function U_{00}^{00} at $k=0.838$ (a.u.); r_1 and r_2 are in units of a_0.

III. FINITE-ELEMENT ANALYSIS OF INELASTIC SCATTERING

A. Modifications to the algorithm

In principle, the treatment of multichannel scattering with the FEM involves nothing more than a change in the asymptotic boundary conditions and an increase in the value of r_c. In practice, this involves a substantial increase in "bookkeeping" and computational effort. In this section, we limit our discussion to inelastic scattering above the $n=2$ threshold, but below the $n=3$ threshold. We discuss only the modifications to the procedure outlined in Sec. II A.

The wave function is now labeled with an additional superscript α to indicate the incident channel of the scattering system. (For the elastic case, only one channel is physically accessible and this index was unnecessary.) The index α represents the asymptotic quantum numbers of the target (n_2,l_2) and the angular momentum of the projectile electron (l_1); we use the designation

α	n_2^α	l_2^α	l_1^α	k^α
1	1	0	L	k
2	2	0	L	κ
3	2	1	$L+1$	κ
4	2	1	$L-1$	κ

where $E=-\frac{1}{2}+k^2/2=-\frac{1}{8}+\kappa^2$. (Note that for $L=0$, there are only three physical channels.)

The wave function $\Psi^{LS\alpha}$ is again expanded in coupled spherical harmonics; we retain the same angular states as for elastic scattering (see Sec. II A). The coupled radial equations are then solved by the FEM. The multichannel nature of the inelastic problem effects only the boundary conditions. For the elastic case, only a single radial component was nonvanishing on the boundary $r_1=r_c$ and it contained a single unknown, the tangent of the phase shift. We now replace Eq. (2.10) with the more complicated boundary condition

$$U_{l_1 l_2}^{LS\alpha}(r_1,r_2)=\sum_\beta \delta_{l_1,l_1^\beta}\delta_{l_2,l_2^\beta}R_{n_2^\beta,l_2^\beta}(r_2)\sqrt{k^\beta} \times[\delta_{\alpha,\beta}j_{l_1^\beta}(k^\beta r_1)+K_{\beta\alpha}j_{-l_1^\beta-1}(k^\beta r_1)] , \tag{3.1}$$

where j_l is the spherical Bessel function, R_{nl} is the hydrogen radial function, and $K_{\beta\alpha}$ is the unknown reactance matrix element. The components of the vector $u^{LS\alpha}$ that correspond to nodes on the boundary are completely determined by Eq. (3.1), except for the four unknown K-matrix elements; the global equation can be rewritten as

$$\tilde{H}^L\tilde{u}^{LS\alpha}=\tilde{c}^{LS\alpha} , \tag{3.2}$$

where

$$\begin{aligned}
&\tilde{H}_{ij}^L=H_{ij}^L, \quad 1\le i\le n+4, \ 1\le j\le n \\
&\tilde{u}_j^{LS\alpha}=u_j^{LS\alpha}, \quad 1\le j\le n \\
&\tilde{u}_{n+\beta}^{LS\alpha}=K_{\beta\alpha}, \quad \beta=1,2,3,4 \\
&\sum_{j=n+1}^{n+4}\tilde{H}_{ij}^L\tilde{u}_j^{LS\alpha}-\tilde{c}_i^{LS\alpha}=\sum_{j=n+1}^{N}H_{ij}^L u_j^{LS\alpha}, \quad 1\le i\le n+4 .
\end{aligned} \tag{3.3}$$

TABLE III. T-matrix elements, cross sections (in πa_0^2) and eigenphase sums as a function of r_c and grid size for $^1S^e$ at $k=0.9$. CPU times (min:sec) are for entire K matrix.

Grid	10×10	14×14	20×20	24×24
r_c	$24a_0$	$40a_0$	$64a_0$	$80a_0$
CPU	3:20	11:57	19:42	36:45
$\lvert T_{11}\rvert^2$	1.864	1.860	1.846	1.851
$\lvert T_{12}\rvert^2$	0.213	0.211	0.203	0.200
$\lvert T_{21}\rvert^2$	0.198	0.204	0.208	0.200
$\lvert T_{13}\rvert^2$	0.069	0.074	0.074	0.074
$\lvert T_{31}\rvert^2$	0.048	0.060	0.075	0.075
$\sigma_{1s\text{-}1s}$	0.575	0.574	0.570	0.571
$\sigma_{1s\text{-}2s}$	0.063	0.064	0.063	0.062
$\sigma_{1s\text{-}2p}$	0.018	0.021	0.023	0.023
$\sum_i \delta_i$	1.765	1.700	1.675	1.681

TABLE IV. Partial-wave cross sections (in πa_0^2) at $k=0.9$. Finite-element results are compared with close-coupling (28 basis functions) [10], R-matrix [7], and finite-difference calculations [8].

State	Method	$\sigma_{1s\text{-}1s}$	$\sigma_{1s\text{-}2s}$	$\sigma_{1s\text{-}2p}$
^1S	close-coupling	0.561	0.059	0.026
	R-matrix	0.564	0.059	0.026
	finite-difference	0.561	0.058	0.028
	finite-element	0.570	0.063	0.023
^3S	close-coupling	3.692	0.0012	0.0006
	R-matrix	3.692	0.0012	0.0006
	finite-element	3.692	0.0013	0.0008
^1P	close-coupling	0.0012	0.0034	0.052
	R-matrix	0.0015	0.0034	0.052
	finite-element	0.0017	0.0048	0.051
^3P	close-coupling	1.979	0.052	0.047
	R-matrix	1.989	0.052	0.048
	finite-element	2.005	0.055	0.047
^1D	close-coupling	0.063	0.060	0.111
	R-matrix	0.063	0.061	0.100
	finite-element	0.063	0.056	0.116
^3D	close-coupling	0.130	0.0027	0.0059
	R-matrix	0.130	0.0027	0.0058
	finite-element	0.131	0.0029	0.0051
^1F	close-coupling	0.010	0.0008	0.0032
	R-matrix	0.011	0.0010	0.0031
	finite-element	0.012	0.0009	0.0033
^3F	close-coupling	0.032	0.0105	0.031
	R-matrix	0.033	0.0096	0.032
	finite-element	0.036	0.0099	0.035

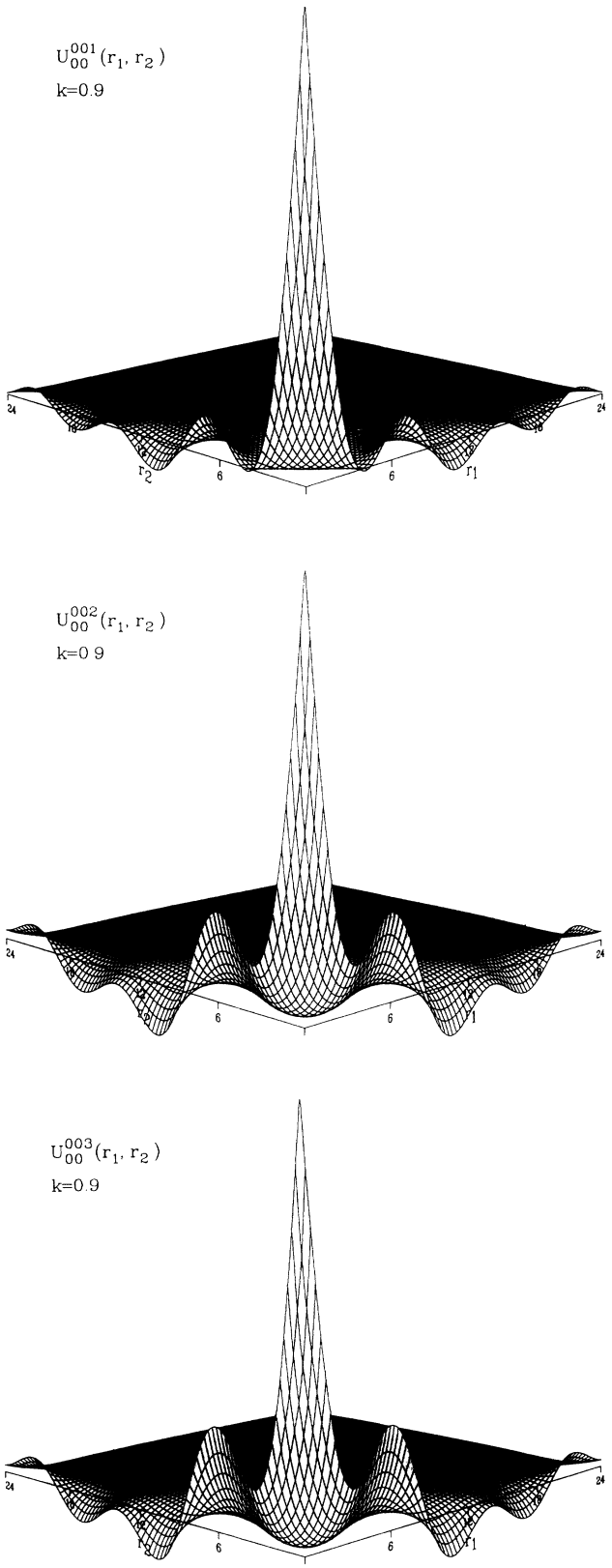

FIG. 3. Radial functions U_{00}^{000}, U_{00}^{001}, and U_{00}^{002} at $k=0.9$ (a.u.), corresponding to the incident target in the 1s, 2s, and 2p states, respectively; r_1 and r_2 are in units of a_0.

The matrix $\tilde{H}$ is of order $(n+4)$, and the last four entries in the vector $\tilde{u}^{LS\alpha}$ are the α column of the K matrix. The FEM calculation is repeated for each incident channel α in order to obtain the full K matrix.

B. Inelastic results

Once the K matrix has been obtained from the solution of Eq. (3.2), it can be used to calculate the T matrix, inelastic cross sections, and eigenphases. In the FEM approach to electron-hydrogen scattering, the symmetry of the K matrix, and consequently the T matrix, is not guaranteed. In fact, the symmetry of the T matrix was used to determine when the radial cutoff r_c was sufficiently large. Typical results are shown in Table III for the $^1S^e$ state at $k=0.9$. Note that although the T matrix was quite nonsymmetric at $r_c=24a_0$ (10×10 grid), the cross sections are still within a few percent of the fully converged values.

The FEM results for partial wave contributions to the cross section for $0\le L\le 3$ are given in Table IV; all results were obtain using $r_c=64a_0$ (20×20 grid). These results are compared with the close-coupling calculation [10], the R matrix [7], and finite difference (for $^1S^e$ only) [8]. There is good agreement between the three calculations for the cross sections $\sigma_{1s\text{-}1s}$, $\sigma_{1s\text{-}2s}$, and $\sigma_{1s\text{-}2p}$, with the exception of the $^1S^e$ state, where the FEM result for $\sigma_{1s\text{-}1s}$ is slightly higher than other calculations.

In Fig. 3, we show the radial functions $U_{00}^{00\alpha}$ for $\alpha=1,2,3$ at $k=0.9$. For the incident channel corresponding to the 1s target, the wave function is similar in structure to the elastic wave function (Fig. 1). In contrast, if the incident target is in a 2s or 2p state, the radial wave function near the nucleus exhibits structure associated with the $n=2$ state of hydrogen and, in the asymptotic region, one can see the superposition of the two free-particle states with $\lambda=2\pi/k$ and $2\pi/\kappa$.

IV. CONCLUSIONS

We have shown that the finite-element method can be successfully used to study both elastic and inelastic scattering. Unlike other approaches, we have avoided the difficulty of long-range couplings among the 1s, 2s, and 2p states by choosing a sufficiently large value of r_c. Thus the finite-element approach is fundamentally different from R-matrix and close-coupling calculations. (The finite-difference calculation of Wang and Callaway [8] included 2s-2p coupling; they have since obtained converged results without asymptotic coupling [11].)

In order to extend finite-element analysis to higher energy, it will be necessary to systematically increase the radial cutoff r_c. In order to prevent CPU times and storage requirements from becoming prohibitively large, new ways of optimizing the finite-element scheme are being investigated. The effect of including asymptotic coupling in the boundary condition is also being studied.

ACKNOWLEDGMENTS

This work has been supported by the National Science Foundation under Grant No. PHY-9024142 (J.S.) and the

U.S. Department of Energy under Grant No. DE-ACOS-840OR21400 (J.B.). This research was conducted using the Cornell National Supercomputer Facility, which receives major funding from the NSF and IBM Corporation. J.S. wishes to thank J. Callaway and T. Scholz for providing partial-wave contributions to inelastic cross sections; J.S. also thanks Y. Wang for providing unpublished finite-difference results without asymptotic coupling. Finally, the help of A. Chandler in preparing the wave-function plots is gratefully acknowledged.

[1] K. J. Bathe, *Finite Element Procedures in Engineering Analysis* (Prentice-Hall, Englewood Cliffs, NJ, 1982); K. J. Bathe and E. Wilson, *Numerical Methods in Finite Element Analysis* (Prentice Hall, Engelwood Cliffs, NJ, 1976).
[2] J. Botero and J. Shertzer, Phys. Rev. A **46**, R1155 (1992).
[3] C. Schwartz, Phys. Rev. **124**, 1468 (1961).
[4] R. L. Armstead, Phys. Rev. A **171**, 91 (1968).
[5] D. Register and R. T. Poe, Phys. Lett. **51A**, 431 (1975).
[6] J. Callaway, Phys. Let. **65A**, 199 (1978).
[7] T. Scholz, P. Scott, and P. G. Burke, J. Phys. B **21**, L139 (1988).
[8] Y. D. Wang and J. Callaway, Phys. Rev. A **48**, 2058 (1993).
[9] Y. K. Ho, Phys. Rev. A **23**, 2137 (1981); J. Phys. B **23**, L71 (1990); A. K. Bhatia and Y. K. Ho, Phys. Rev. A **41**, 504 (1990).
[10] J. Callaway, Phys. Rev. A **26**, 199 (1982); **37**, 3692 (1988).
[11] Y. D. Wang (private communication).

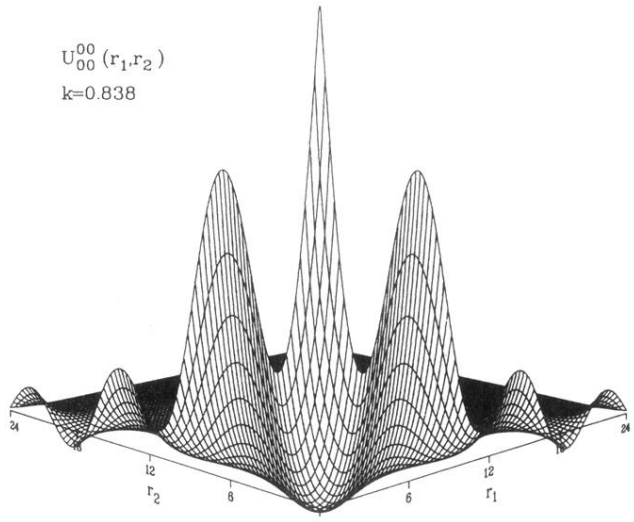

FIG. 2. Radial function U_{00}^{00} at $k=0.838$ (a.u.); r_1 and r_2 are in units of a_0.

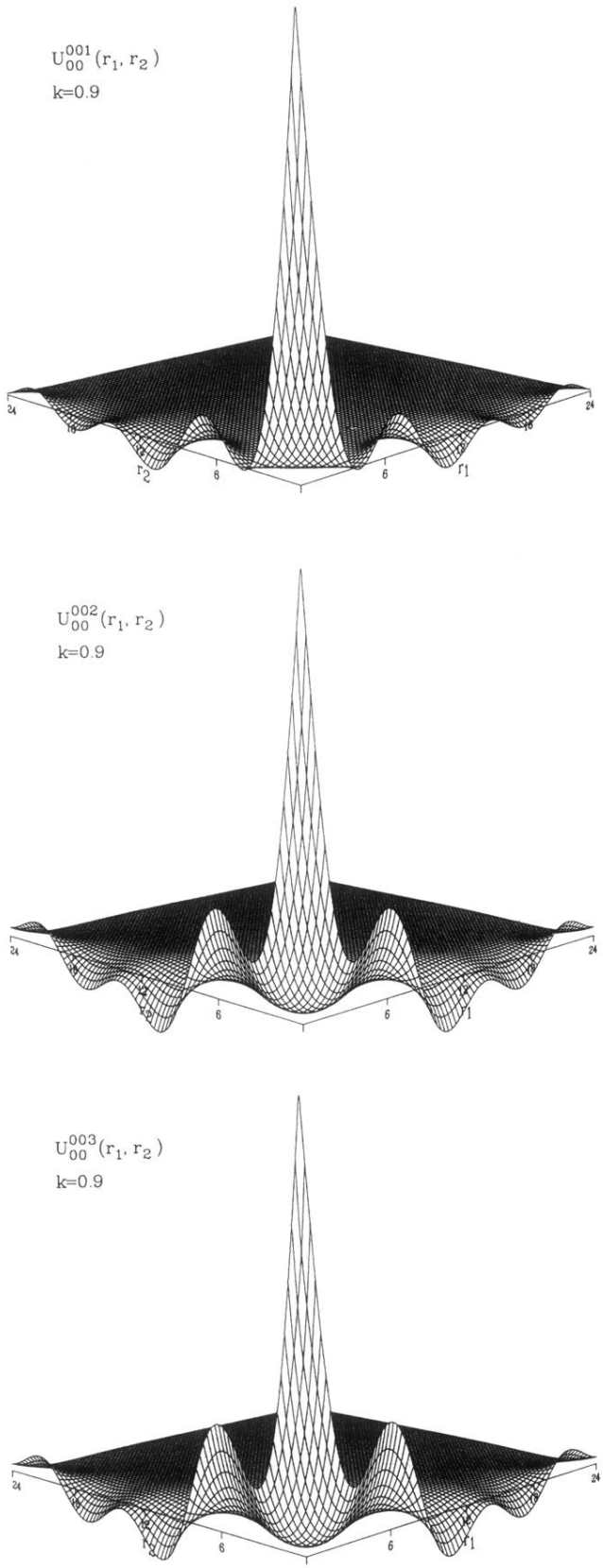

FIG. 3. Radial functions U_{00}^{000}, U_{00}^{001}, and U_{00}^{002} at $k=0.9$ (a.u.), corresponding to the incident target in the 1*s*, 2*s*, and 2*p* states, respectively; r_1 and r_2 are in units of a_0.